Understanding the effects of transition metal intercalation on electronic and electrochemical properties of $Ti_3C_2T_x$ MXene

Shianlin Wee[1], Xiliang Lian[2†], Evgeniya Vorobyeva[1†], Akhil Tayal[3], Vladimir Roddatis[4], Fabio La Mattina[5], Dario Gomez Vazquez[1], Netanel Shpigel[6], Mathieu Salanne[2,7], Maria R. Lukatskaya[1]*

[1] Electrochemical Energy Systems Laboratory, Department of Mechanical and Process Engineering, ETH Zurich, 8092 Zurich, Switzerland.
[2] Physicochimie des Électrolytes et Nanosystèmes Interfaciaux, PHENIX, Sorbonne Université, CNRS, F-75005 Paris, France.
[3] Deutsches Elektronen-Synchrotron DESY, Notkestrasse 85, Hamburg D-22607, Germany.
[4] Helmholtz Centre Potsdam, GFZ German Research Centre for Geosciences, 14473 Potsdam, Germany.
[5] Empa - Swiss Federal Laboratories for Materials Science and Technology, 8600 Dübendorf, Switzerland.
[6] The Institute of Chemistry, The Hebrew University of Jerusalem, Jerusalem, 919040, Israel.
[7] Institut Universitaire de France (IUF), 75231 Paris, France.

† Equal contribution

* Corresponding author email: mlukatskaya@ethz.ch

ABSTRACT

MXenes are 2D transition metal carbides, nitrides, and/or carbonitrides, capable of intercalation by various cations through chemical or electrochemical means. Previous research has primarily focused on intercalating alkaline and alkaline earth cations, such as Li^+, K^+, Na^+, Mg^{2+} or alkylammonium cations, into $Ti_3C_2T_x$ MXenes. However, the impact of intercalated transition metal (TM) ions on the electronic and electrochemical properties of MXenes remains largely unexplored. In this study, we investigated the effects of pre-intercalated Cu ions on $Ti_3C_2T_x$ MXenes and vice versa to gain a comprehensive understanding of how the electronic and electrochemical properties of both intercalated TM ion and MXene host are altered. Using in-situ X-ray absorption spectroscopy (XAS), we reveal changes in the oxidation states of intercalated Cu ions and Ti atoms during charging and their corresponding role in charge storage mechanisms. Our findings show that electronic coupling between $Ti_3C_2T_x$ and Cu ions results in modified electrochemical and electronic properties compared to pristine $Ti_3C_2T_x$. These insights lay the foundation for the rational design and utilization of TM ion intercalants to tailor the properties of MXenes for various electrochemical systems and beyond.

INTRODUCTION

MXenes are a family of two-dimensional (2D) transition metal carbonitrides[1] with a general formula of $M_{n+1}X_nT_x$, where *M* is an early transition metal, $n = 1 – 4$; *X* is carbon and/or nitrogen and T_x refers to surface termination such as =O, -OH, -Cl, -F etc.).[2-4] MXenes offer a unique combination of tunable metallicity[1, 5] and hydrophilicity[1, 5-7] coupled with attractive redox properties that gave rise to their promise in numerous applications from fast energy storage[5, 8-15] and electrocatalysis[16-17] to biomedical[18-20] and electromagnetic shielding[21]. Electronic and electrochemical properties of MXenes can be tailored by changing the chemistry of MXenes: from the type of transition metals (TMs) constituting the *MX* layer to modification of the surface terminations.[1, 22-24] Further, since MXenes are layered and have negatively charged surfaces,[9, 25-26] they can be (electro-)chemically intercalated by a range of cations and polar molecules[1, 9, 27-29]offering an additional tuning knob to alter their physicochemical properties[22, 30]. Intercalation of various types of cations was reported: monovalent (Li^+, Na^+, K^+, NH_4^+)[9, 12, 31], multivalent (Mg^{2+}, Al^{3+}, Sn^{4+})[9, 12, 32-34] and organic cations (alkylammonium (TBA)[12, 29, 35]). However, in the literature of MXenes, very few studies focus on the intercalation of TM cations in MXenes and/or target the elucidation of the charge storage mechanisms occurring in the TM-intercalated MXene. Yet, intercalation of TM cations into semi-metallic MXenes represents a unique scenario since redox-active intercalants can offer distinct reactivities and cause charge redistribution within MXene layers, and thus, altering its electronic properties and electrochemical responses.[17] For example, immobilization of single Pt atoms on Mo vacancies in $Mo_2TiC_2T_x$ MXene enabled excellent electrocatalytic performance and stability of the material.[17] This was attributed to the favorable changes in electronic structure of both $Mo_2TiC_2T_x$ MXene and Pt single atoms that resulted in the enhanced hydrogen evolution electrocatalytic activity.[17] While recently a few more reports of TM intercalation in MXenes appeared[36-38], a general mechanistic understanding is still lacking on the fundamental interactions between such redox active TM intercalants and MXene.

Herein, we probe the effects of pre-intercalated Cu ions on $Ti_3C_2T_x$ and vice versa, with the goal of providing a comprehensive understanding of how the physicochemical and electrochemical properties of both pre-intercalated transition metal cation and MXene itself are altered through a combination of X-ray absorption spectroscopy (XAS) and four-point probe techniques, as well as ab initio molecular dynamics (AIMD) and Density Function theory (DFT) calculations. Specifically, we apply in-situ XAS, to track the oxidation changes of both intercalated Cu ions and Ti atoms of the MXene under different applied potentials, providing insights into the charge transfer between Cu ions and $Ti_3C_2T_x$. We show that the interactions between $Ti_3C_2T_x$ and Cu ions resulted in altered electronic and electrochemical properties compared to the Cu^{2+} ions in solution and pristine $Ti_3C_2T_x$. Using Cu ions and $Ti_3C_2T_x$ MXene as an example, this work offers a mechanistic understanding of the interactions between intercalated transition metal cations and MXene layers, providing foundation for the rational design and utilization of transition metal ion intercalants to tune properties of MXenes for their applications in different electrochemical systems and beyond.

RESULTS AND DISCUSSION

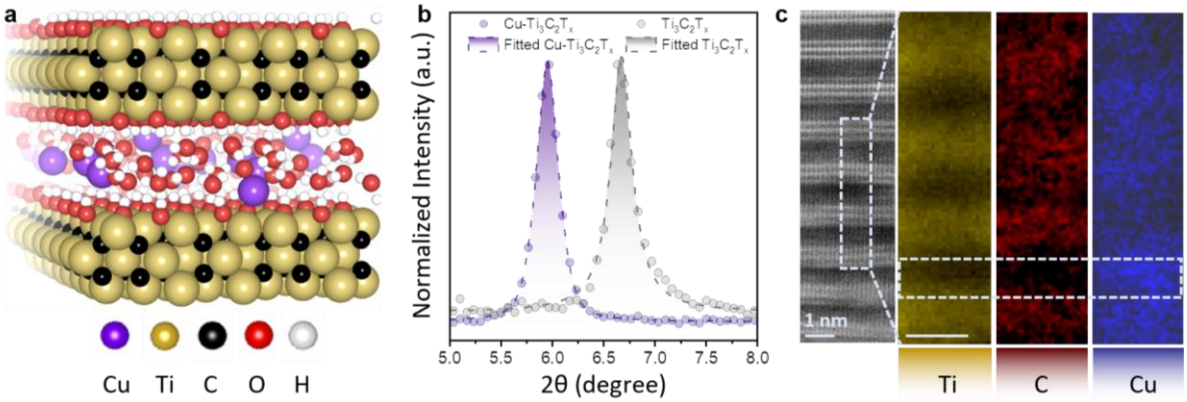

Figure 1 (a) Final structure of Cu-$Ti_3C_2T_x$ MXene generated from *ab initio* molecular dynamics (AIMD) calculation. (b) X-ray diffraction (XRD) patterns of pristine and Cu-intercalated $Ti_3C_2T_x$. (c) High-resolution transmission electron microscopy (HR-TEM) image with the corresponding electron energy loss spectroscopy (EELS) atomic maps of Ti, C and Cu elements of Cu-$Ti_3C_2T_x$.

Characterization of Cu-$Ti_3C_2T_x$

First, the Cu-intercalated $Ti_3C_2T_x$ MXene was synthesized following the Ghidiu et al. method (detailed procedure description in Experimental Section).[39] The successful intercalation of Cu ions was verified by X-ray diffraction (XRD) analysis: the (002) peak experienced shift to the lower angle (2θ = 6.0°) corresponding to a larger d-spacing of 14.8 Å compared to pristine $Ti_3C_2T_x$ (2θ = 6.7°, d-spacing of 13.2 Å)[40] (**Figure 1b, Figure S1**). High resolution electron energy loss spectroscopy (EELS) mapping (**Figure 1c**) coupled with scanning transmission electron microscopy (STEM) – energy dispersive X-ray spectroscopy (EDX) maps (**Figure S3**) revealed the homogeneous distribution of Cu in between $Ti_3C_2T_x$ layers. The quantification of the intercalated Cu-ion fraction was carried out using inductively coupled plasma - optical emission spectrometry (ICP), revealing an average of Cu content of 0.23 ± 0.007 per each $Ti_3C_2T_x$ unit (**Figure S2**), these values are closely comparable with the values from STEM-EDX. Importantly, the absence of Cu nanoparticles on the MXene surfaces was confirmed by STEM-EDX imaging (**Figure S3**), SEM-EDX imaging (**Figure S3**), and XRD (**Figure S1**). These results establish the successful intercalation of Cu ions within the $Ti_3C_2T_x$ structure.

Next, we investigated the chemical state of intercalated Cu-ions using X-ray absorption spectroscopy (XAS) (**Figure 2a**) and AIMD. Cu-$Ti_3C_2T_x$ XANES spectra lacks a typical pre-edge feature that is a known signature of the Cu^{2+} presence (d^9 electronic configuration, classic 1s → 3d transition) (**Figure S4**).[41] Moreover, Cu absorption edge energy in Cu-$Ti_3C_2T_x$ sample resides between those of Cu_2O (Cu^{1+}) and CuO (Cu^{2+}), indicating that electron density around Cu-ions changed significantly upon intercalation in MXene. Further, to provide a quantitative estimate of oxidation state of intercalated Cu-ions, we compared XANES spectra of Cu-$Ti_3C_2T_x$, Cu_2O, and CuO, and the corresponding edge energy was plotted *vs.* Cu oxidation state in known Cu compounds (**Figure S5**). Using interpolation, an average oxidation state of Cu-ions is estimated to be ~ +1.3. This correlates well with charge redistribution observed from the density functional theory (DFT) calculations (**Figure 2d**): while from DFT the oxidation number is not a direct observable[42], however, an estimation of the partial charge of Cu atoms provided by the Bader analysis (**Table S1**) of Cu-$Ti_3C_2T_x$ DFT model yields a value of ~ + 0.42 |e|. This matches the Bader charge of Cu in bulk Cu_2O (+0.52 |e|), which indicates a more reduced state of intercalated Cu ions compared to Cu^{2+} in the solution.

In contrast, Ti K-edge energy of Cu-intercalated Ti_3C_2 shifted by ~0.41 eV towards more positive values compared to pristine $Ti_3C_2T_x$ (**Figure 2b**, **Figure S6**). As such, we hypothesize that Cu-ion intercalation induces charge redistribution, pulling some of the electron density on itself from MXene layers.[17, 43] To probe the effect of Cu intercalation on the electronic properties of MXenes, we performed temperature-dependent electrical conductivity measurements of both Cu-$Ti_3C_2T_x$ and $Ti_3C_2T_x$ MXene pellets. Notably, Cu-intercalated MXene exhibited >2 orders of magnitude increase in resistivity compared to pristine $Ti_3C_2T_x$ (**Figure 2c**). Although cation intercalation can lead to increased inter-flake resistivity (and hence overall resistivity) in MXenes as a result of enlarged interlayer spacing, it is important not to overlook the role of intercalant nature and chemistry.[44-45] It is important to note that despite of the resistivity increase for Cu-$Ti_3C_2T_x$, the material can still be classified as electrically conductive. In agreement with that, DFT calculations show that the Density of States (DOS) is not significantly altered by the Cu ion intercalation (**Figure 2d**) as the electronic states associated to the latter are below the Fermi level.

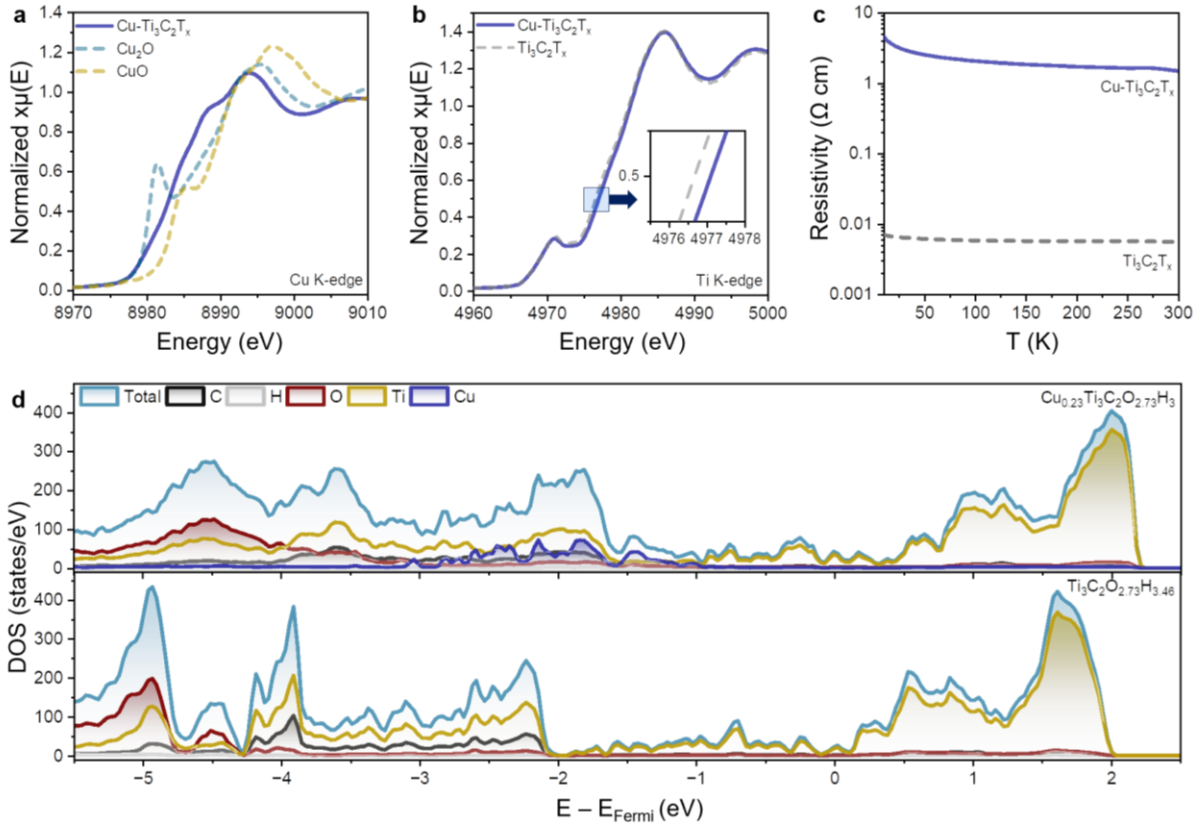

Figure 2 (a) Normalized X-Ray absorption spectra of Cu-$Ti_3C_2T_x$, Cu_2O and CuO at Cu K-edge. (b) Normalized X-Ray absorption spectra of Cu-$Ti_3C_2T_x$ and $Ti_3C_2T_x$ at Ti K-edge. (c) Temperature dependence of resistivity of pellets from Cu-$Ti_3C_2T_x$ and $Ti_3C_2T_x$ powders. (d) Density of States (DOS) of the $Cu_{0.23}Ti_3C_2O_{2.73}H_3$ (upper panel) and $Ti_3C_2O_{2.73}H_{3.46}$ (lower panel) MXenes obtained from DFT calculations.

Electrochemical response of Cu-$Ti_3C_2T_x$

Electrochemical response of the Cu-intercalated $Ti_3C_2T_x$ is characterized by the distinct cyclic voltammetry profile with additional redox peak at ~-0.6 V *vs*. Ag/AgCl compared to $Ti_3C_2T_x$, suggesting the participation of intercalated Cu ions in the charge storage mechanism (**Figure 3a**). To further examine the possible redox contributions of Cu ions, we performed *in-situ* XAS to probe the possible changes in Cu K-edges of Cu-$Ti_3C_2T_x$ at different applied potentials ranging from -0.45 V to -1.25 V *vs.* Ag/AgCl. In the XANES region, a highly reversible shift of the Cu K-edge energy towards lower energies was observed during cathodic scan, corresponding to a partial reduction of Cu ions (**Figure 3b, c**). Concurrently, the overall electrode resistance decreases, as observed from the electrochemical impedance spectra (EIS) collected at different reducing potentials (**Figure 3d**). We estimate that on average, each Cu ion gains ~0.2 e^- during charging (**Figure S7**). It is also important to note that, despite applied charging potentials being significantly more reducing than Cu^0/Cu^{2+} (-0.44 V versus Ag/AgCl)[46] or Cu^0/Cu^+ (-0.58 V vs Ag/AgCl[46]) standard reduction potentials, Cu ions in Cu-$Ti_3C_2T_x$ do not undergo full reduction to metallic state, further indicating that electrons are delocalized between conductive MXene matrix and Cu intercalants.

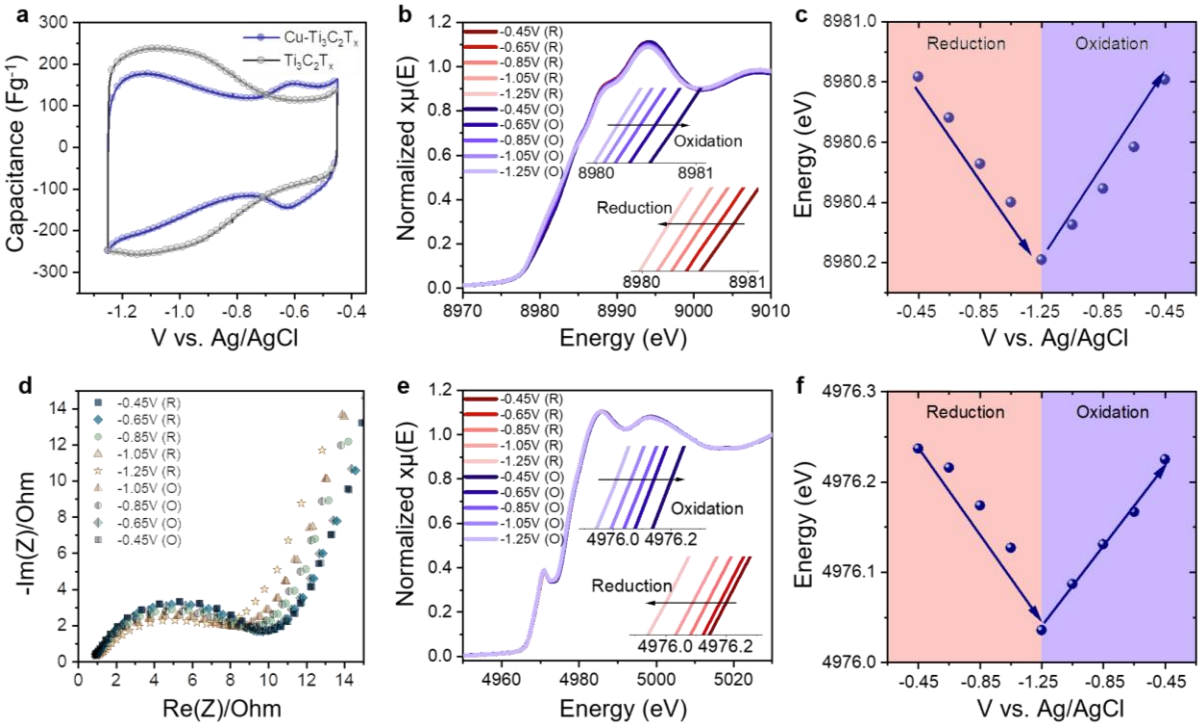

Figure 3. (a) Cyclic voltammetry profiles of Cu-$Ti_3C_2T_x$ and $Ti_3C_2T_x$ at 0.5mVs^{-1}. (b-c) Electrochemical XAS data of Cu-$Ti_3C_2T_x$ where (b) Cu K-edge XANES spectra at different applied potentials and (c) Variation of Cu edge energy (at 0.27 normalized XANES spectra) vs potential during negative and positive potential sweep. (d) Electrochemical impedance spectroscopy (EIS) of Cu-$Ti_3C_2T_x$ collected at different applied potentials. (e) Ti K-edge XANES spectra of Cu-$Ti_3C_2T_x$ measured at different applied potential. (f) Variation of Ti edge energy (at half height of normalized XANES spectra) with applied potential.

Complementary to monitoring the changes in the Cu K-edge energies as a function of potential, we also examined the corresponding changes in Ti K-edge energies to obtain a more comprehensive insight of the charge storage mechanism in Cu-$Ti_3C_2T_x$. Similar to the trend observed in the case of Cu K-edge, the Ti XANES spectra also displayed highly reversible shifts towards lower energy (decrease in Ti oxidation state) during the negative scan (**Figure 3e & f**). By correlating edge energy shifts to the Ti

valency, we estimate that each $Ti_3C_2T_x$ unit gains ~0.18 e^- during charging over the potential window of 0.8 V (**Figure S8**). Hence, according to XAS, each $Cu_{0.23}Ti_3C_2T_x$ unit gains an estimated 0.22 e^- during charging, corresponding to the redox capacitance of 125 F g^{-1}. This value is quite close to the capacitance value obtained from electrochemical measurements in Swagelok cell: 145 F g^{-1}. Therefore, we can infer that both Ti of MXene layer and intercalated Cu ions actively participate in charge storage and majorly contribute to the overall capacitance. It is also worth noting that the observed XAS changes in the oxidation states of Ti (**Figure 3e**) also serve as a direct indication of the pseudocapacitive nature of charge storage mechanism for $Ti_3C_2T_x$ in alkaline electrolytes, similar to the earlier proven mechanism observed in acidic electrolytes.[47-48] This effectively refutes a hypothesis that the lower capacitance $Ti_3C_2T_x$ observable in alkaline and neutral electrolytes stems predominantly from electrical double-layer capacitance.[25]

CONCLUSIONS

In summary, we demonstrate that the electronic and electrochemical properties of MXenes can be altered through the intercalation of redox-active TM cations. Specifically, we reveal a distinct difference in electrochemical response of the Cu-$Ti_3C_2T_x$ compared to pristine MXene and provide the evidence for the participation of both intercalated Cu ions and Ti of MXene in the charge storage. We attribute this to the redistribution and delocalization of electrons between MXene matrix and intercalated Cu ions. Our results demonstrate a reciprocal interplay between TM intercalant and MXene host, wherein they exert a synergistic effect on each other properties and hence providing an additional avenue to tune MXene properties through TM intercalation. Finally, our findings highlight the significant contribution of Ti redox to the Cu-$Ti_3C_2T_x$ capacitance, thereby confirming the pseudocapacitive charge storage mechanism of $Ti_3C_2T_x$ in alkaline electrolytes.

MATERIALS AND METHODS

Synthesis of $Ti_3C_2T_x$. Cu-intercalated $Ti_3C_2T_x$ and $Ti_3c_2T_x$ MXene were synthesized following Ghidiu et al. procedure.[39-40] Specifically, 1 g of Ti_3AlC_2 powder (Carbon-Ukraine, <44 µm particle size) was gradually added to a 10 ml solution of 10 wt% hydrofluoric acid (HF, Sigma-Aldrich, 48 wt%) and ~1.1 g LiCl (with a molar ratio 5:1 to Ti_3AlC_2). Then, the mixture was stirred at 300 rpm for 24 hours at room temperature. This step leads to the simultaneous selective removal of Al layer from Ti_3AlC_2 and the intercalation of Li^+ ions in between $Ti_3C_2T_x$ layers. Next, the wet sediment was divided into two batches and washed 3 times with 6 M HCl (hydrochloric acid, Sigma-Aldrich, 37%) with a ratio of 0.5 g MXene to 40 ml of HCl solution. After each washing, centrifugation at 3500 rpm for 5 min was performed. This yielded the $Ti_3C_2T_x$ MXene in which intercalated Li^+ ions were exchanged by H_3O^+. Finally, the sediment was washed with 40 ml MiliQ water at least 4 times until pH 5 was reached. For the control sample – non-intercalated "pristine" $Ti_3C_2T_x$ – the wet sediment was collected directly after DI washing and dried and used as is for the experiments.

Preparation of Cu-intercalated $Ti_3C_2T_x$. For the intercalation of Cu ions, 40 ml of 0.1 M copper (II) sulphate pentahydrate ($CuSO_4 \bullet 5H_2O$, Carl Roth, 99%) was added to 0.5 g of wet $Ti_3C_2T_x$ sediment. The mixture was hand shaken for 2 min and left to rest for 1 hour. After centrifugation at 3500 rpm for 5 mins, the supernatant was removed and replaced with a fresh 0.1 M $CuSO_4$ solution. Then, the mixture was left for another 24 hours under continuous stirring at 300 rpm and Ar bubbling at room temperature. Finally, the sediment was washed three times with MiliQ water, collected via vacuum filtration and dried under vacuum for 24 hours.

Electrode preparation. The electrodes were prepared following the procedure described in references[9, 49]. The working electrode was composed of 90 wt.% of MXene powder, 5 wt.% of polytetrafluoroethylene binder (PTFE, Sigma-Aldrich) and 5 wt.% of carbon black (CB, Orion). The counter electrode contained 95 wt.% of activated carbon (MTI) and 5 wt.% of polytetrafluoroethylene binder (PTFE, Sigma-Aldrich).

X-ray diffraction patterns were acquired using PANalytical Empyrean X-ray Powder Diffractometer with Cu K_α radiation at 40 mA and 40 kV. The powders were scanned in 2θ range from 4.5° to 60°, with an acquisition step of 0.067° and 700 s per step in reflection geometry.

Scanning transmission electron microscopy (STEM) images with the corresponding ***energy-dispersive X-ray spectroscopy (EDX)*** mapping were collected at 200 kV for 5 mins on FEI Talos F200X microscope and equipped with an FEI SuperX detector (Chem S/TEM, ScopeM, ETH Zurich). Samples for scanning transmission electron microscopy were prepared by grounding sample and dusting the powder onto standard nickel mesh lacey carbon support films (EMresolutions, Quantifoil).

High resolution TEM images and Electron Energy Loss Spectroscopy (EELS) maps were collected on cross-section TEM lamellas that were prepared with a lift-out method using a Thermo Fisher Scientific (TFS, former FEI) Helios G4 UC Focused Ion Beam (FIB) instrument. Further, the lamellas were studied using a Cs aberration-corrected at the probe side TEM (TFS Themis Z 80-300, operated at 300 kV, equipped with a Gatan Continuum 1065 Electron Energy Loss Spectrometer). Both Helios G4 UC and Themis Z microscopes are a part of Potsdam Imaging and Spectral Analysis facility (PISA).

Scanning electron microscopy (SEM) images with the corresponding ***EDX*** analysis were collected using Hitachi S-4800 microscope at 20 kV for 5 mins. A thin layer of MXene powder was spread on the carbon tape. Excess powder was removed with compressed air.

Inductively coupled plasma optical emission spectrometry (ICP-OES) measurements were conducted with an Agilent 720 ES instrument. The ICP sample preparation involved the addition of approximately 5 – 8 mg of Cu-$Ti_3C_2T_x$ powders (stored in dry box) to a 10 ml solution of 20 wt.% HNO_3 (Sigma-Aldrich, 70%) at room temperature for at least 24 hours under continuous stirring (100 rpm) until complete dissolution was achieved. After that, the solution was diluted until concentration of 10 wt.% HNO_3 was reached. Prior to each measurement, instrument calibrations were performed using solutions of $CuSO_4$ (Carl Roth, 99%) in a 10 wt.% HNO_3 with concentrations of 0, 10, 50, and 100 ppm of Cu ions where the signals were recorded at the most prominent emission wavelength of 327.395 nm.

Resistivity measurements. Utilizing a Quantum Design Physical Property Measurement System (PPMS), resistivity measurements were conducted over a temperature range of 4 K to 300 K. For these measurements, we utilized MXene pellets that were prepared using a standard laboratory press at room temperature and a pressure of 20 MPa. These pellets were cut into rectangular stripes for the measurement. On each pellet, four gold (Au) electrode pads, each measuring between 50 - 100 nm in thickness and 0.1 mm in width, were deposited with a Leica EM ACE200 sputter coater. These pads were 2.5 mm apart. Indium wires were subsequently attached to the Au pads, creating a 4-probe geometry. To ensure optimal electrical contact, a small amount of silver (Ag) paint was additionally applied at the contact points.

Electrochemical set-up and measurements. Cyclic voltammetry (CV) and electrochemical impedance spectroscopy (EIS) were performed using Biologic MPG-200 and VSP-300 potentiostats, respectively, with a three-electrode Swagelok cell configuration. MXene electrode served as working electrode with glassy-carbon disk as a current collector (CH instruments), while activated carbon electrode served as counter electrode with Ti rod as a current collector and an Ag/AgCl in 1M KCl (CH instruments) as reference electrode. 1 M NaOH (Sigma-Aldrich, ⩾98%) electrolyte and one layer of polypropylene separator (Celgard 3501) were used to assemble the cell. CV was performed at the scan rate of 0.5 mVs^{-1} while EIS was measured at open circuit voltage in frequency range from 100 kHz to 100 mHz, with an amplitude of 10 mV and 6 points per decade.

X-ray absorption spectroscopy (XAS) measurements were performed at P64 Advanced X-ray Absorption Spectroscopy beamline in Deutsches Elektronen (DESY) Synchrotron (Hamburg, Germany), using a Si (111) monochromator. Samples were prepared by mixing ~4 mg of powder sample with ~60 mg of cellulose (Sigma-Aldrich), and made into a 1-mm-thick pellets that are 13 mm in diameter using a pelletizer die set at 5 ton-force. These pellets were measured in transmission mode for Ti K-edge, while Cu K-edge measurements were performed in fluorescence geometry using passivated implanted planar silicon (PIPS) detector (positioned at 90° angle relative to the incident X-ray). For each pellet, data was collected for about 2 mins around Ti K-edge (4.96 keV) and Cu K-edge (8.97 keV); a total of 5 acquisitions for both transmission and fluorescence signals were collected. Energy calibration for each spectrum was performed using Cu (edge at 8.97 keV) and Ti (edge at 4.96 keV) foils. The data was averaged for 5 acquisitions and analyzed using Athena software. The Cu edge energy for each sample was defined as energy at the normalized intensity of 0.27 (this intensity corresponds to the

zero of the 2nd derivative[50-52] and a maximum of the 1st derivative[53] for Cu foil spectrum). The Ti edge energy position was extracted based on the half height of the normalized intensity of spectrum[47, 50, 53] which is close to the zero of the 2nd derivative.[50-52]

In-situ X-ray Absorption Spectroscopy (XAS) was performed using a Si (111) monochromator and PIPS detector, at P64 Advanced X-ray Absorption Spectroscopy beamline at DESY Synchrotron (Hamburg, Germany). Both Ti K-edge (4.96 keV) and Cu K-edge (8.97 keV) were collected in fluorescence mode, where the PIPS detector was position at 45° relative to the MXene electrode in the in-situ cell. A three-electrode in-situ cell (ECC-Opto-Std test cell, EL-cell, Germany) was used: a 50 nm Au evaporated on 1-mm-thick polyetherimide sheet was utilized as both cell's X-Ray window and a current collector for Cu-intercalated $Ti_3C_2T_x$ MXene working electrode (90% MXene, 5% PTFE, 5% CB). Overcapacitive activated carbon served as counter electrode, leakless Ag/AgCl with filling electrolyte 3.4 M KCl (eDAQ) served as reference electrode and one layer of polypropylene separator (Celgard 3501) was used during the cell assembly. Prior XAS measurement, the cell was precycled at 1 mVs^{-1} for 3 CV cycles between -0.45 V and -1.25 V vs Ag/AgCl. Next, for in-situ XAS data acquisition, a linear sweep voltammetry (LSV) followed by about 15 min potential hold were performed for each potential of interest (-0.45 V, -0.65 V, -0.85 V, -1.05 V, -1.25 V). The in-situ XAS data were collected for at least 10 minutes in total during potential hold and at least 3 spectra were collected at each potential.

The data analysis was performed using Athena software. The Cu and Ti edge positions were defined as specified above. An estimation of the Cu oxidation state for Cu-$Ti_3C_2T_x$ samples was performed by referencing edge energy and Cu valence to those of reference compounds Cu_2O (Sigma-Aldrich, ⩾99.99%) and CuO (Sigma-Aldrich, ⩾99.0%) (**Figure S7**). The changes of the Ti oxidation state were assessed in a similar manner, using TiO (Alfa Aesar, 99.5%) and TiO_2 rutile (Sigma-Aldrich, 99.5%) reference compounds (**Figure S8).**

The valency changes obtained from Cu and Ti XANES spectra were further correlated with the experimental capacitance values calculated from cyclic voltammetry. To estimate charge storage contributions from Ti and Cu redox the following formula: $C_g = \frac{zF}{M_w V}$ was used, where C_g [F g^{-1}] refers to gravimetric capacitance, z corresponds to the number of electrons participating in the electrochemical reaction, F [96485 C mol^{-1}] is the Faraday's constant, M_w [g mol^{-1}] is the molar weight and V [V] is the potential window. The electrochemical reaction occurred is assumed as followed:

$$Cu_{0.23}Ti_3C_2O_x(OH)_yF_{2-x-y} + \delta e^- + \delta Na^+ \rightarrow Cu_{0.23}Ti_3C_2O_x(OH)_yF_{2-x-y}Na_\delta$$

In the case of Cu, the number of electrons participating is equal to 0.19 × 0.23 = 0.04; while for Ti, the number of electrons participating is equal to 0.06 × 3 = 0.18. Assuming the molecular weight of 215.5 g mol^{-1} for $Cu_{0.23}Ti_3C_2T_x$, capacitance of 125 F g^{-1} was estimated as a result of Cu and Ti redox contributions. This matches very well with the experimental capacitance of 145 F g^{-1} (calculated from CV).

Density functional theory (DFT) calculation and molecular dynamics (MD) simulation. The electronic structure calculations were performed within the density functional theory framework as implemented in Vienna ab initio simulation package (VASP)[54-55]. The wavefunctions were expanded in plane wave basis sets and projector augmented wave (PAW) method. The exchange-correlation energy was approximated with the generalized gradient approximation as formulated by Perdew, Burke, and Ernzerhof (PBE)[56]. The MXene structure with single-water layer was simulated following the procedure reported in reference.[57] To lower the computational cost, we reduced the a and b

dimensions where our final $Ti_3C_2T_x$ structure contains 90 Ti atoms, 60 C atoms, 82 O atoms, and 104 H atoms. Then, the Cu^{2+} ions were added step-by-step, followed by geometry optimization to stabilize the structure. Experimentally, each $Ti_3C_2T_x$ unit corresponds to 0.23 ± 0.007 Cu, therefore we inserted 7 Cu atoms into the water layer with 14 H atoms randomly removed concurrently. For structural optimization, we set the kinetic energy cutoff to 520 eV and sampled the Brillouin zone with a k-spacing of 0.3 $Å^{-1}$. The electronic convergence threshold is set to 10^{-6} eV and the forces are converged to 0.05 eV $Å^{-1}$. The Cu ions-intercalated structure was then equilibrated using AIMD for 40 ps and we computed the Bader charges[58], and the density of states (DOS) based on the final structure. The AIMD calculations were performed with an NVT ensemble, where we fix the number of atoms, volume and temperature and with a timestep of 1 fs. Gamma point was used to sample Brillouin zone with a reduced cutoff energy of 450 eV to make the computation more affordable.

ACKNOWLEGMENT:

M. R. L., S.W. acknowledge support from the ETH Foundation. S.W. acknowledges for provision of synchrotron radiation beamtime at beamline at P64 Advanced X-ray Absorption Spectroscopy beamline in Deutsches Elektronen Synchrotron DESY. The authors thank the European Regional Development Fund and the State of Brandenburg for the Themis Z TEM (part of Potsdam Imaging and Spectral Analysis (PISA)). This work was granted access to the HPC resources of CINES under Allocation A0140910463 made by GENCI.

REFERENCES

[1] B. Anasori, M. R. Lukatskaya, Y. Gogotsi, *Nature Reviews Materials* **2017**, *2*, 16098.

[2] X. Li, Z. Huang, C. E. Shuck, G. Liang, Y. Gogotsi, C. Zhi, *Nature Reviews Chemistry* **2022**, *6*, 389-404.

[3] M. Naguib, O. Mashtalir, M. R. Lukatskaya, B. Dyatkin, C. Zhang, V. Presser, Y. Gogotsi, M. W. Barsoum, *Chemical Communications* **2014**, *50*, 7420-7423.

[4] A. Lipatov, M. Alhabeb, M. R. Lukatskaya, A. Boson, Y. Gogotsi, A. Sinitskii, *Advanced Electronic Materials* **2016**, *2*, 1600255.

[5] O. Mashtalir, M. R. Lukatskaya, M.-Q. Zhao, M. W. Barsoum, Y. Gogotsi, *Advanced Materials* **2015**, *27*, 3501-3506.

[6] J. Halim, M. R. Lukatskaya, K. M. Cook, J. Lu, C. R. Smith, L.-Å. Näslund, S. J. May, L. Hultman, Y. Gogotsi, P. Eklund, M. W. Barsoum, *Chemistry of Materials* **2014**, *26*, 2374-2381.

[7] H. Ghassemi, W. Harlow, O. Mashtalir, M. Beidaghi, M. R. Lukatskaya, Y. Gogotsi, M. L. Taheri, *Journal of Materials Chemistry A* **2014**, *2*, 14339-14343.

[8] M. Ghidiu, M. R. Lukatskaya, M.-Q. Zhao, Y. Gogotsi, M. W. Barsoum, *Nature* **2014**, *516*, 78-81.

[9] M. R. Lukatskaya, O. Mashtalir, C. E. Ren, Y. Dall'Agnese, P. Rozier, P. L. Taberna, M. Naguib, P. Simon, M. W. Barsoum, Y. Gogotsi, *Science* **2013**, *341*, 1502-1505.

[10] M. R. Lukatskaya, S. Kota, Z. Lin, M.-Q. Zhao, N. Shpigel, M. D. Levi, J. Halim, P.-L. Taberna, M. W. Barsoum, P. Simon, Y. Gogotsi, *Nature Energy* **2017**, *2*, 17105.

[11] Y. Dall'Agnese, M. R. Lukatskaya, K. M. Cook, P.-L. Taberna, Y. Gogotsi, P. Simon, *Electrochemistry Communications* **2014**, *48*, 118-122.

[12] M. D. Levi, M. R. Lukatskaya, S. Sigalov, M. Beidaghi, N. Shpigel, L. Daikhin, D. Aurbach, M. W. Barsoum, Y. Gogotsi, *Advanced Energy Materials* **2015**, *5*, 1400815.

[13] O. Mashtalir, M. R. Lukatskaya, A. I. Kolesnikov, E. Raymundo-Piñero, M. Naguib, M. W. Barsoum, Y. Gogotsi, *Nanoscale* **2016**, *8*, 9128-9133.

[14] M.-Q. Zhao, C. E. Ren, Z. Ling, M. R. Lukatskaya, C. Zhang, K. L. Van Aken, M. W. Barsoum, Y. Gogotsi, *Advanced Materials* **2015**, *27*, 339-345.

[15] C. Zhang, M. Beidaghi, M. Naguib, M. R. Lukatskaya, M.-Q. Zhao, B. Dyatkin, K. M. Cook, S. J. Kim, B. Eng, X. Xiao, D. Long, W. Qiao, B. Dunn, Y. Gogotsi, *Chemistry of Materials* **2016**, *28*, 3937-3943.

[16] Z. W. Seh, K. D. Fredrickson, B. Anasori, J. Kibsgaard, A. L. Strickler, M. R. Lukatskaya, Y. Gogotsi, T. F. Jaramillo, A. Vojvodic, *ACS Energy Letters* **2016**, *1*, 589-594.

[17] J. Zhang, Y. Zhao, X. Guo, C. Chen, C.-L. Dong, R.-S. Liu, C.-P. Han, Y. Li, Y. Gogotsi, G. Wang, *Nature Catalysis* **2018**, *1*, 985-992.

[18] M. Soleymaniha, M.-A. Shahbazi, A. R. Rafieerad, A. Maleki, A. Amiri, *Advanced Healthcare Materials* **2019**, *8*, 1801137.

[19] A. Zamhuri, G. P. Lim, N. L. Ma, K. S. Tee, C. F. Soon, *BioMedical Engineering OnLine* **2021**, *20*, 33.

[20] M. Zimmermann, L.R.H. Gerken, S. Wee, V. M. Kissling, A. L. Neuer, E. Tsolaki, A. Gogos, M. R. Lukatskaya, I. K. Herrmann, *ChemRxiv* **2023**.

[21] F. Shahzad, M. Alhabeb, C. B. Hatter, B. Anasori, S. Man Hong, C. M. Koo, Y. Gogotsi, *Science* **2016**, *353*, 1137-1140.

[22] J. L. Hart, K. Hantanasirisakul, A. C. Lang, B. Anasori, D. Pinto, Y. Pivak, J. T. van Omme, S. J. May, Y. Gogotsi, M. L. Taheri, *Nature Communications* **2019**, *10*, 522.

[23] B. Anasori, C. Shi, E. J. Moon, Y. Xie, C. A. Voigt, P. R. C. Kent, S. J. May, S. J. L. Billinge, M. W. Barsoum, Y. Gogotsi, *Nanoscale Horizons* **2016**, *1*, 227-234.

[24] M. A. Hope, A. C. Forse, K. J. Griffith, M. R. Lukatskaya, M. Ghidiu, Y. Gogotsi, C. P. Grey, *Physical Chemistry Chemical Physics* **2016**, *18*, 5099-5102.

[25] J. Xu, J. You, L. Wang, Z. Wang, H. Zhang, *Sustainable Materials and Technologies* **2022**, *33*, e00490.

[26] N. Shpigel, A. Chakraborty, F. Malchik, G. Bergman, A. Nimkar, B. Gavriel, M. Turgeman, C. N. Hong, M. R. Lukatskaya, M. D. Levi, Y. Gogotsi, D. T. Major, D. Aurbach, *Journal of the American Chemical Society* **2021**, *143*, 12552-12559.
[27] J. Li, H. Wang, X. Xiao, *Energy & Environmental Materials* **2020**, *3*, 306-322.
[28] Q. Gao, W. Sun, P. Ilani-Kashkouli, A. Tselev, P. R. C. Kent, N. Kabengi, M. Naguib, M. Alhabeb, W.-Y. Tsai, A. P. Baddorf, J. Huang, S. Jesse, Y. Gogotsi, N. Balke, *Energy & Environmental Science* **2020**, *13*, 2549-2558.
[29] M. Ghidiu, S. Kota, J. Halim, A. W. Sherwood, N. Nedfors, J. Rosen, V. N. Mochalin, M. W. Barsoum, *Chemistry of Materials* **2017**, *29*, 1099-1106.
[30] J. Come, J. M. Black, M. R. Lukatskaya, M. Naguib, M. Beidaghi, A. J. Rondinone, S. V. Kalinin, D. J. Wesolowski, Y. Gogotsi, N. Balke, *Nano Energy* **2015**, *17*, 27-35.
[31] N. Shpigel, M. R. Lukatskaya, S. Sigalov, C. E. Ren, P. Nayak, M. D. Levi, L. Daikhin, D. Aurbach, Y. Gogotsi, *ACS Energy Letters* **2017**, *2*, 1407-1415.
[32] S. Li, Q. Shi, Y. Li, J. Yang, T.-H. Chang, J. Jiang, P.-Y. Chen, *Advanced Functional Materials* **2020**, *30*, 2003721.
[33] Y. Li, Y. Deng, J. Zhang, Y. Han, W. Zhang, X. Yang, X. Zhang, W. Jiang, *Nanoscale* **2019**, *11*, 21981-21989.
[34] C. Wang, S. Chen, H. Xie, S. Wei, C. Wu, L. Song, *Advanced Energy Materials* **2019**, *9*, 1802977.
[35] K. Liang, R. A. Matsumoto, W. Zhao, N. C. Osti, I. Popov, B. P. Thapaliya, S. Fleischmann, S. Misra, K. Prenger, M. Tyagi, E. Mamontov, V. Augustyn, R. R. Unocic, A. P. Sokolov, S. Dai, P. T. Cummings, M. Naguib, *Advanced Functional Materials* **2021**, *31*, 2104007.
[36] Y. Bai, C. Liu, T. Chen, W. Li, S. Zheng, Y. Pi, Y. Luo, H. Pang, *Angewandte Chemie International Edition* **2021**, *60*, 25318-25322.
[37] Y.-H. Chen, M.-Y. Qi, Y.-H. Li, Z.-R. Tang, T. Wang, J. Gong, Y.-J. Xu, *Cell Reports Physical Science* **2021**, *2*, 100371.
[38] D. Zhang, S. Wang, R. Hu, J. Gu, Y. Cui, B. Li, W. Chen, C. Liu, J. Shang, S. Yang, *Advanced Functional Materials* **2020**, *30*, 2002471.
[39] M. Ghidiu, J. Halim, S. Kota, D. Bish, Y. Gogotsi, M. W. Barsoum, *Chemistry of Materials* **2016**, *28*, 3507-3514.
[40] L. Verger, V. Natu, M. Ghidiu, M. W. Barsoum, *The Journal of Physical Chemistry C* **2019**, *123*, 20044-20050.
[41] B. L. Geoghegan, Y. Liu, S. Peredkov, S. Dechert, F. Meyer, S. DeBeer, G. E. Cutsail, III, *Journal of the American Chemical Society* **2022**, *144*, 2520-2534.
[42] A. Walsh, A. A. Sokol, J. Buckeridge, D. O. Scanlon, C. R. A. Catlow, *Nature Materials* **2018**, *17*, 958-964.
[43] W. Lin, Y.-R. Lu, W. Peng, M. Luo, T.-S. Chan, Y. Tan, *Journal of Materials Chemistry A* **2022**, *10*, 9878-9885.
[44] A. Al-Temimy, K. Prenger, R. Golnak, M. Lounasvuori, M. Naguib, T. Petit, *ACS Applied Materials & Interfaces* **2020**, *12*, 15087-15094.
[45] J. Halim, S. Kota, M. R. Lukatskaya, M. Naguib, M.-Q. Zhao, E. J. Moon, J. Pitock, J. Nanda, S. J. May, Y. Gogotsi, M. W. Barsoum, *Advanced Functional Materials* **2016**, *26*, 3118-3127.
[46] P. Vanýsek, *CRC Handbook of Chemistry and Physics*, 91 ed., **2010**.
[47] M. R. Lukatskaya, S.-M. Bak, X. Yu, X.-Q. Yang, M. W. Barsoum, Y. Gogotsi, *Advanced Energy Materials* **2015**, *5*, 1500589.
[48] C. Zhan, M. Naguib, M. Lukatskaya, P. R. C. Kent, Y. Gogotsi, D.-e. Jiang, *The Journal of Physical Chemistry Letters* **2018**, *9*, 1223-1228.
[49] M. R. Lukatskaya, D. Feng, S.-M. Bak, J. W. F. To, X.-Q. Yang, Y. Cui, J. I. Feldblyum, Z. Bao, *ACS Nano* **2020**, *14*, 15919-15925.
[50] C. Christov, *Biomolecular Spectroscopy: Advances from Integrating Experiments and Theory*, Elsevier Science, **2013**.

[51] T. A. Roelofs, W. Liang, M. J. Latimer, R. M. Cinco, A. Rompel, J. C. Andrews, K. Sauer, V. K. Yachandra, M. P. Klein, *Proc Natl Acad Sci U S A* **1996**, *93*, 3335-3340.
[52] J. Yano, V. K. Yachandra, *Photosynthesis Research* **2009**, *102*, 241-254.
[53] S. Calvin, *XAFS for Everyone*, CRC Press, **2013**.
[54] G. Kresse, J. Furthmüller, *Physical Review B* **1996**, *54*, 11169-11186.
[55] G. Kresse, D. Joubert, *Physical Review B* **1999**, *59*, 1758-1775.
[56] J. P. Perdew, K. Burke, M. Ernzerhof, *Physical Review Letters* **1996**, *77*, 3865-3868.
[57] N. C. Osti, M. Naguib, A. Ostadhossein, Y. Xie, P. R. C. Kent, B. Dyatkin, G. Rother, W. T. Heller, A. C. T. van Duin, Y. Gogotsi, E. Mamontov, *ACS Applied Materials & Interfaces* **2016**, *8*, 8859-8863.
[58] G. Henkelman, A. Arnaldsson, H. Jónsson, *Computational Materials Science* **2006**, *36*, 354-360.